Article

# Coherent control of a superconducting qubit using light

Hana K. Warner [1] ✉, Jeffrey Holzgrafe[1,5], Beatriz Yankelevich [2,6],
David Barton [1,7], Stefano Poletto [2], C. J. Xin [1], Neil Sinclair[1], Di Zhu [1],
Eyob Sete[2], Brandon Langley[2], Emma Batson[3], Marco Colangelo [3,8],
Amirhassan Shams-Ansari[1], Graham Joe[1], Karl K. Berggren [3], Liang Jiang [4],
Matthew J. Reagor [2,9] & Marko Lončar [1] ✉

Quantum communications technologies require a network of quantum processors connected with low-loss and low-noise communication channels capable of distributing entangled states. Superconducting microwave qubits operating in cryogenic environments have emerged as promising candidates for quantum processor nodes. However, scaling these systems is challenging because they require bulky microwave components with high thermal loads that can quickly overwhelm the cooling power of a dilution refrigerator. Telecommunication frequency optical signals, however, can be fabricated in significantly smaller form factors to avoid challenges caused by high signal loss, noise sensitivity and thermal loads due to their high carrier frequency and propagation in silica optical fibres. Transduction of information by means of coherent links between optical and microwave frequencies is therefore critical to leverage the advantages of optics for superconducting microwave qubits, while also enabling superconducting processors to be linked with low-loss optical interconnects. Here, we demonstrate coherent optical control of a superconducting qubit. We achieve this by developing a microwave–optical quantum transducer that operates with up to 1.18% conversion efficiency with low added microwave noise, and we demonstrate optically driven Rabi oscillations in a superconducting qubit.

Superconducting (SC) qubits and SC quantum circuits have emerged as one of the most promising quantum computing (QC) platforms and have been used to demonstrate processing advantages over classical supercomputers, even in the presence of system noise[1,2]. However, to reach the true potential of this platform, systems containing hundreds of logical qubits (many thousands of physical qubits) are required[3]. This is challenging because SC qubits require ultra-low temperatures to operate, and this large number of qubits would result in prohibitively large dilution refrigerators with cooling power that cannot be achieved with current technology[4]. One approach to overcome this relies on a modular computing scheme[5,6] based on a network of small-scale quantum processors, each in its own refrigerator, connected with low-noise and low-loss quantum links. As SC qubits can be accessed using microwave photons in the frequency range ~3–8 GHz, SC quantum links between dilution refrigerators could be used to allow the transmission of microwave signals. However, this requires cryogenically

[1]Harvard John A. Paulson School for Engineering and Applied Sciences, Cambridge, MA, USA. [2]Rigetti Computing, Berkeley, CA, USA. [3]Research Laboratory of Electronics, Massachusetts Institute of Technology, Cambridge, MA, USA. [4]Pritzker School of Molecular Engineering, University of Chicago, Chicago, IL, USA. [5]Present address: Hyperlight Corporation, Cambridge, MA, USA. [6]Present address: Research Laboratory of Electronics, Massachusetts Institute of Technology, Cambridge, MA, USA. [7]Present address: Department of Materials Science and Engineering, Northwestern University, Evanston, IL, USA. [8]Present address: Electrical and Computer Engineering Department, Northeastern University, Boston, MA, USA. [9]Present address: Google LLC, Mountain View, CA, USA. ✉e-mail: hwarner@g.harvard.edu; loncar@seas.harvard.edu
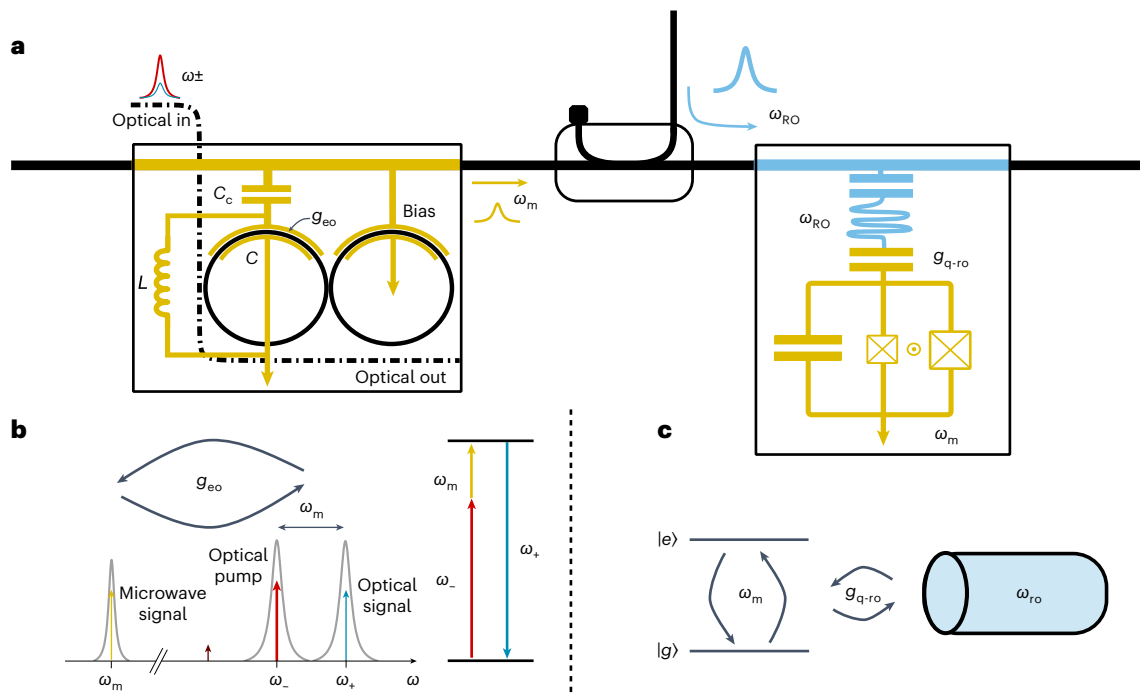
Fig. 1 | Transducer-driven superconducting qubit scheme. a, Two optical fields ($\omega_{\pm}$) are coupled into the transducer by means of a waveguide. The two modes are resonant with the transducer's hybridized optical modes which are generated by a coupled paperclip resonator capacitively coupled (C_C) to a microwave LC resonator ($\omega_m = \frac{1}{\sqrt{LC}}$). The optical modes interact in the transducer to generate a microwave tone (ω_m) by means of difference frequency generation using the $\chi^{(2)}$ nonlinearity in TFLN according to the microwave–optical coupling rate g_{eo}. The microwave tone is then transmitted to an SC qubit chip by means of a coaxial cable to drive the qubit through a dispersively coupled readout resonator. We determined the qubit state by measuring the transmission of a readout pulse (ω_{ro}) generated at room temperature. **b**, Schematic of CEO transduction process. Two hybridized optical modes ($\omega_{\pm}$) are detuned by the microwave resonance frequency (ω_m). Energy exchange between the microwave and optical domains was mediated by the strong pump field at ω_-. **c**, The qubit computational ground ($|g\rangle$) and excited ($|e\rangle$) states are separated by frequency ω_m. The qubit is dispersively coupled to a microwave readout resonator (ω_{ro}) with strength $g_{q\text{-}ro}$.

cooled (<50 mK) links between each subsystem[7], which is challenging, costly and not scalable.

An alternative approach relies on interfacing SC qubits with photons at telecommunication frequencies (~200 THz), propagating in low-loss optical fibres. Optical photons have much higher energy than microwave photons and thus are insensitive to thermal noise even at room temperature. Furthermore, their high carrier frequency and large bandwidth allow wavelength-division multiplexing, resulting in a 100-fold increase in the number of addressable physical qubits in a single fibre. Moreover, because silica optical fibres are weak carriers of thermal energy, they could be used to replace traditional microwave coaxial cables[8] to provide a 1,000× reduction in thermal load for signals routed in and out of a refrigerator. Finally, optical fibre-based quantum links between SC processors benefit from mature classical optical communication technology and could enable efficient, low-noise and high-rate quantum interconnects between quantum processors over kilometres[9]. This reach can be further extended by combining processors with emerging quantum-repeater-based quantum networks[10].

A key component needed to interface SC qubits with light is a microwave–optical quantum transducer (MOQT), which is a device capable of providing a coherent, bidirectional link while preserving fragile quantum states across five orders of magnitude of energy. This is challenging owing to the lack of a strong coherent nonlinearity that can bridge this vast energy gap between microwave and optical photons. Microwave–optical quantum transduction has been pursued using several approaches[11–13]. Piezoelectric optomechanical[14–16], membrane optomechanical[17] and cavity electro-optic (CEO)[18–21] platforms have shown particular promise in recent years due to demonstrations of low-noise performance[17,22,23], single-photon operation[18,24,25] and bidirectional conversion[14,15,17,22,26,27]. Furthermore, recent demonstrations

of optical driving[8] and readout of SC qubits[8,28–30] demonstrate the potential to reduce passive heat load and space requirements to enable further scaling of SC processors, with high-fidelity SC qubit readout in piezoelectric optomechanical[29] and all-optical SC qubit readout in bulk electro-optic[30] platforms illustrating the potential for near-term scaling of SC qubit systems with MOQTs.

CEO-MOQTs, which leverage a strong Pockel's effect in materials with large χ^2 nonlinearities, are especially of interest due to the direct conversion process between the microwave and optical domains, which circumvents potential lossy, noisy or rate-limiting intermediary modes that can limit transduction bandwidth. Among these, the thin-film lithium niobate (TFLN) photonic platform has emerged as a front runner[13,20,21] because it combines a large electro-optic (EO) coefficient ($r_{33} \approx 30$ pm V^{-1}), the ability to realize ultra-high Q optical resonators[31,32] and wafer-scale fabrication processes[33].

Despite great progress, CEO-MOQTs still require strong pump powers, which can lead to increased noise and limit the device repetition rates (to maintain low bath temperature)[18,23], with open questions on the influence of scattered optical light and d.c. flux noise on the performance of SC qubits.

Here, we overcome these limitations and demonstrate a TFLN-CEO-MOQT design and use it to demonstrate coherent optical driving of a SC qubit (Fig. 1a). The transducer is a triply resonant system[34] that consists of an on-chip microwave LC resonator operating at frequency ω_m which is capacitively coupled by means of the EO effect to two coupled optical resonators that give rise to hybridized optical modes at frequencies ω_+ and $\omega_- = \omega_+ - \omega_m$ (ref. 35). This allows a resonantly enhanced exchange of energy between the microwave and optical modes. In our approach, an optical pump (ω_-) and idler (ω_+) interact at a CEO-MOQT to generate a microwave signal at the qubit frequency (ω_m) by means of a difference frequency generation process (Fig. 1b).
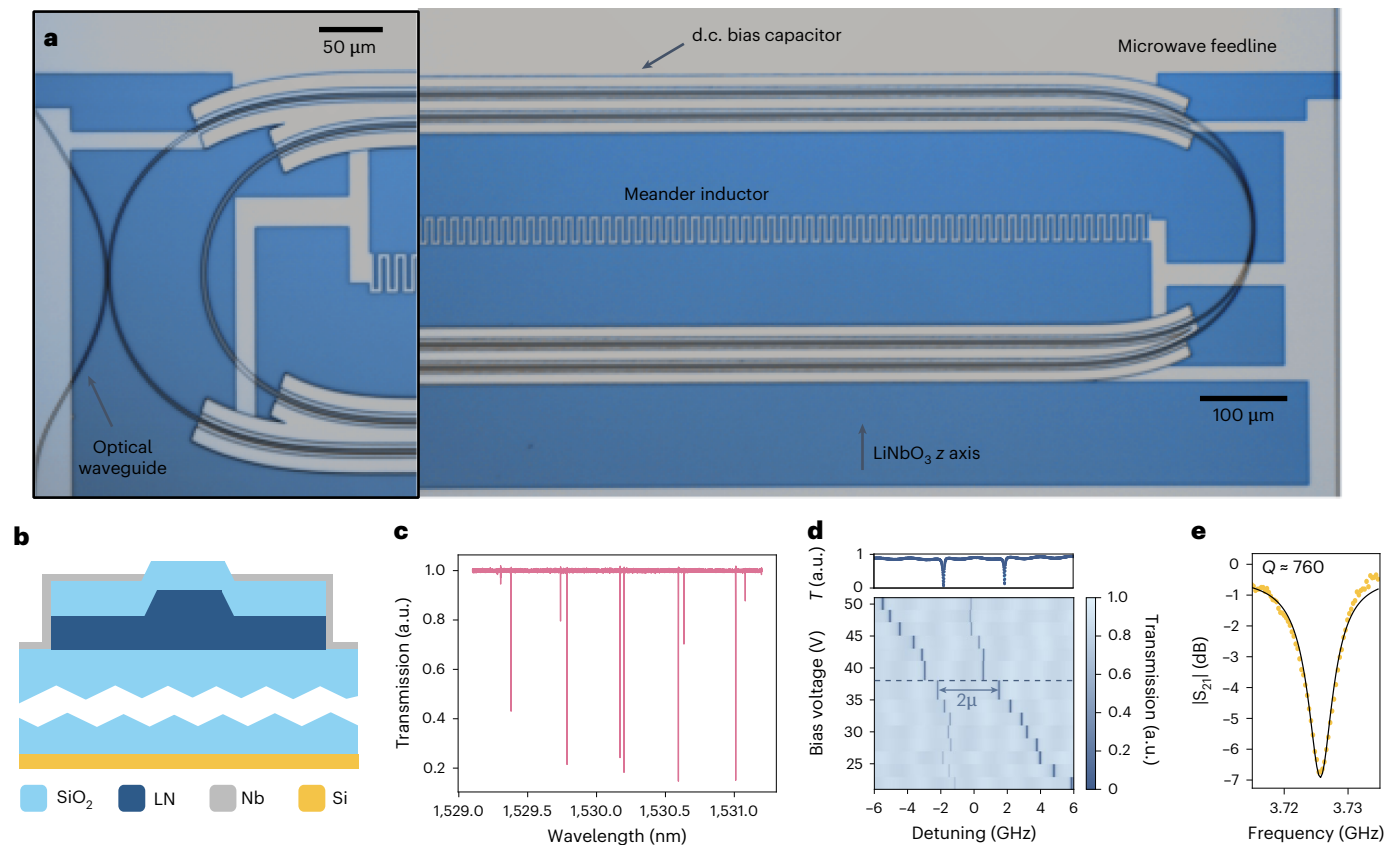
Fig. 2 | CEO-MOQT. a, Optical micrograph of transducer. An Nb microwave LC resonator (silver) was capacitively coupled to two hybridized LN racetrack resonators in a paperclip geometry (black) to coherently exchange energy between the microwave and optical domains using the resonantly enhanced EO effect in LN. This geometry allowed us to have a small device footprint to lower parasitic capacitance. The device was cladded with silica to aid with thermal dissipation and mitigate optical losses due to electrical crossovers. The microwave signal was read out by means of a transmission line (top), and the optical signal was collected by means of optical grating couplers (Extended Data Fig. 2). The optical racetrack resonators adiabatically tapered from 1 μm in coupling regions to 3 μm in the straight section of the racetrack to reduce sidewall scattering losses while supporting only the fundamental transverse mode (inset). **b**, Drawing of device cross-section. Our optical waveguides were gated in a plateau-like electrode geometry to directly contact our Nb electrodes with the z axis of the LN crystal, and thus benefit from the large Pockel's coefficient ($r_{33} \approx 30$ pm V^{-1}). This improved microwave–optical field overlap, and thus the single-photon coupling rate, between our microwave and optical modes. **c**, The nested paperclip geometry resulted in a Vernier effect with 5 nm periodicity and ensured the existence of a pair of hybridized optical modes with splitting similar to the microwave resonant frequency. **d**, We could then ensure that we operated at the triple-resonance point by controlling the optical detuning with a voltage bias ($2\mu \approx 3.5$ GHz) to match our microwave resonator frequency ($\omega_m \approx 3.7$ GHz) shown in **e**, the microwave transmission measured through the device.

The microwave pulse was then transmitted by means of a coaxial cable to a qubit in the same refrigerator ($T_{CEO\text{-}MOQT} \approx T_{qubit} \approx 15$ mK). The qubit was dispersively coupled to a readout resonator (ω_{ro}), which allowed the readout of the qubit state by means of a quantum non-demolition measurement, by measuring the transmission of a readout pulse[36] (Fig. 1c). The cooperation of a thin-film CEO-MOQT and an SC qubit allowed us to characterize the impact of the thin-film CEO-MOQT operation on the SC qubit and validate near-term utility of TFLN EO transducers for optically interfacing with SC qubits.
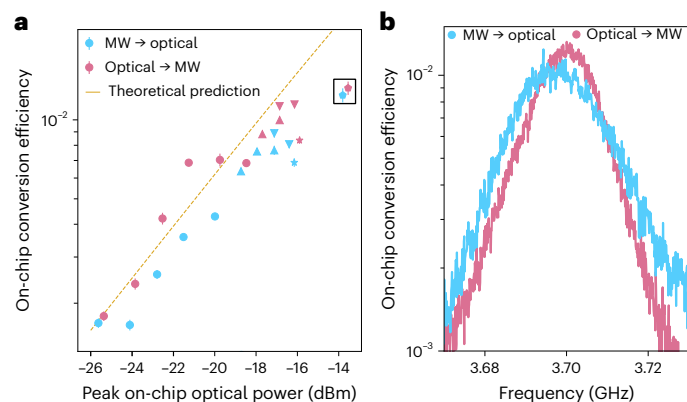
EO transducer characterization

Our transducer was realized using coupled optical racetrack resonators in a paperclip configuration (Fig. 2a), which supported hybridized optical modes that were delocalized between the two racetrack resonators and featured a characteristic split resonance.

The paperclip resonator allowed us to maintain a low parasitic capacitance owing to the small device footprint. Our optical resonators featured a 1 μm-wide optical waveguide in the coupling regions to prevent exciting higher-order transverse modes. The waveguide was then adiabatically expanded to 3 μm in straight sections of the cavities to minimize intrinsic optical losses caused by sidewall roughness ($\kappa_{o,i}/2\pi \approx 25$ MHz), yielding a total optical loss of $\kappa_o/2\pi \approx 80$ MHz.

Waveguides were patterned using a negative-tone e-beam resist (hydrogen silsesquioxane FOx-16) and etched using Ar+ plasma ion etching. After etching, devices were annealed in a 520 °C oxygen environment to mitigate defects in as-received LN or accumulated during the etching process. They were then cladded with IC-PECVD silicon dioxide and re-annealed at 520 °C in O$_2$ to mitigate hydrogen defects in the device oxide cladding that would result in excess optical losses[32]. Next, windows in our oxide layer surrounding optical waveguides were created using a combination of Ar$^+$ and CF$_4$ reactive ion etching. Niobium (Nb) was then sputtered and patterned using negative-tone photoresist (SPR 700-1.0) and etched using CF$_4$ reactive ion etching to create the superconducting electrodes needed to realize our microwave LC resonator and transmission lines. This allowed us to use a plateau-like electrode geometry (Fig. 2b), in which our electrodes were in direct contact with the z axis of the LiNbO$_3$ crystal to enhance the microwave–optical field overlap. This improved our simulated microwave–optical coupling rate by 40% compared with a fully cladded device structure and increased the rate of coherent exchange of energy between the optical and microwave signals (Extended Data Fig. 1). Furthermore, direct contact between lithium niobate (LN) and metal is known to mitigate charge screening effects and d.c. bias drift[37], enabling a more stable operation at the triple-resonance condition.

Fig. 3 | Characterization of transducer performance. a, On-chip conversion efficiency for MW → Optical (blue, sum frequency generation) and Optical → MW (pink, difference frequency generation) measured for different peak on-chip optical-pump powers. The roll-off in conversion efficiency was attributed to optical-pump-induced quasiparticle generation in our superconductor resulting in excess loss in our microwave resonator and drift away from the triply resonant condition. The ∘ markers correspond to CW optical signals, whereas other shapes correspond to a 150 ns pulse, with △ representing a 1 MHz repetition rate (15% duty cycle), ▽ representing a 500 kHz repetition rate (7.5% duty cycle), ⋆ representing a 333 kHz repetition rate (5% duty cycle) and a pentagon representing a 200 kHz repetition rate (2% duty cycle). The theoretical peak conversion efficiency assuming uniform optical and microwave loss rates is plotted as a dotted gold line. **b**, A frequency-dependent efficiency sweep for a 150 ns pulse with 200 kHz duty cycle is highlighted in the black box in **a**.

A 191-μm mismatch in the length of the coupled racetrack resonators was introduced to create a 4 GHz (31 pm) difference in free-spectral range, which resulted in a Vernier effect for our optical modes (Fig. 2c) with 5 nm periodicity. This resulted in different coupling and frequency splitting (anticrossing) for different modes and ensured that some of the hybridized mode pairs featured a resonance split close to the microwave resonator frequency. Then, moderate d.c. bias voltages ($|V_{d.c.}| < 50$ V), compatible with our cryogenic bias-tee at the mixing chamber plate of the refrigerator, were applied to bias the electrode to fine tune the resonance splitting by means of the EO effect and to achieve our triple-resonance condition (Fig. 2d).

Our LC microwave resonator was designed to be blue-detuned by a few megahertz from the desired microwave frequency $\omega_m = \omega_+ - \omega_-$ to compensate for the red-shifting and broadening it experienced under strong optical pumping due to small but finite optical absorption in our superconductor. The device reported here had a microwave frequency $\omega_m/2\pi \leq 3.71$ GHz (Fig. 2e) and a minimal optical mode splitting $2\mu \approx 3.5$ GHz (Fig. 2d). We operated our device with a d.c. voltage bias $V_{d.c.} \approx 36$ V.

To characterize the efficiency of the bidirectional transduction process (η), we excited the paperclip resonator with a strong optical pump resonant with our red optical mode ($\omega_- \approx 193$ THz). For optical-to-microwave conversion, we also excited the paperclip resonator with a weaker optical idler resonant with the blue optical mode (ω_+), that was derived from the pump using a single-sideband modulator. The idler power was 20 dB lower than the pump power so as to remain in the red-pumping regime. The two modes interacted in the transducer to generate a microwave signal at the microwave resonator frequency by means of difference frequency generation ($\omega_m = \omega_+ - \omega_-$), which we measured on a network analyser after -70 dB of link gain. In the microwave–optical conversion regime, a microwave tone generated by the network analyser interacted with the red pump to generate a blue optical signal by means of sum frequency generation ($\omega_+ = \omega_- + \omega_m$). The on-chip microwave power was kept low, with uniform power $P_m \approx -80$ dBm. We measured the beatnote of the optical signal

against an optical pump on a calibrated InGaAs detector to extract the flux of the optical signal and characterize conversion in the microwave–optical regime (Methods). The device was characterized in the continuous-wave (CW) and pulsed-optical regimes. The pulsed regime enabled larger peak optical powers to be applied while avoiding negative photorefractive effects or thermal bath heating. Square optical pulses were generated by modulating the state of our optical fields by an acousto-optic modulator driven by an arbitrary-waveform generator. Pulses were then amplified by an erbium-doped fibre amplifier before being sent to the transducer. In the pulsed-optical regime, we chose our optical pulse width and duty cycle to maintain a low thermal bath temperature ($T_{bath} \leq 30$ mK). See Extended Data Fig. 3 for further details on the measurement system.

In Fig. 3a, we show the on-chip conversion efficiency for different peak on-chip optical powers and duty cycles in the range 2–15%. For pulsed measurements, we maintained a pulse width of 150 ns with pulse frequency changing from 1 MHz to 200 kHz. A smaller duty cycle is beneficial for keeping average optical power in the refrigerator low, whereas a high repetition rate can result in faster operation of the transducer. We extracted the conversion efficiency per microwatt of pump to be ~0.05% μW⁻¹ in the linear operating regime of our superconductor. We note that, particularly in the CW regime, the optical pump could have a dramatic effect on our microwave resonator linewidth. This was largely mitigated in the pulsed regime by maintaining a low average optical power. More details can be found in Extended Data Fig. 4. In current experiments, the peak conversion efficiency measured both in the microwave → optical (MW → Optical) and optical → microwave (Optical → MW) conversion regimes was $\eta \approx 1.18\%$ for −13.8 dBm (44.2 μW) of on-chip optical power (Fig. 3a). We note that this was a 400-fold improvement over our previous result[20] and a 500-fold improvement in conversion per microwatt of pump power when compared with other integrated photonics EO transducers[21,23]. Our transducer also featured a bidirectional 3 dB bandwidth up to 30 MHz (Fig. 3b). This was extracted by sweeping the frequency applied to the single-sideband modulator using a network analyser. The roll-off in converted power measured at high optical-pump powers corresponded to a distortion of our microwave resonator due to finite absorption of the superconductor resulting in nonlinear behaviour, as well as drift in our triple-resonance condition during measurement.

From efficiency and linewidth measurements, we could extract the microwave–optical coupling rate (g_{eo}) and cooperativity (C) to understand the coherence of our system, given $C = \frac{4g_{eo}^2 n_-}{\kappa_+ \kappa_m}$. Here, $n_- = \frac{\kappa_{-,e}}{\kappa_-^2/2} \frac{P_{pump}}{\hbar\omega_-}$ is our intracavity photon number corresponding to the red optical pump for input power P_{pump} and optical (extrinsic) decay rate $\kappa_{-,(e)} = 70$ (48.5) MHz. The loss rate of the blue optical signal field was described by $\kappa_+ = 90$ MHz, and the pump-power-dependent decay of the microwave signal field was described by $\kappa_m > 7$ MHz (values reported in Extended Data Fig. 4a). We found that the $g_{eo}/2\pi \approx 945$ Hz and measured cooperativity up to 1.16%.

We next evaluated the optically induced microwave noise generated by the transducer. To improve the signal-to-noise ratio for these measurements, we characterized the device using the schematic shown in Fig. 4a and measured the output power spectral density (PSD) on a real-time spectrum analyser (RSA).

We calibrated our link gain (G) and noise photons in our system (N_{sys}) using a variable temperature black-body (V_{BB}) source which followed the temperature distribution[22]

$$P_{avg} \approx \frac{1}{2} G\hbar\omega_m \text{BW} \coth\left(\frac{\hbar\omega_m}{2k_B T_{V_{BB}}}\right) \quad (1)$$

for source temperature $T_{V_{BB}}$ and noise bandwidth BW. Because the black-body source was connected directly to the transducer, we assumed that the waveguide was also thermalized at temperature $T_{V_{BB}}$
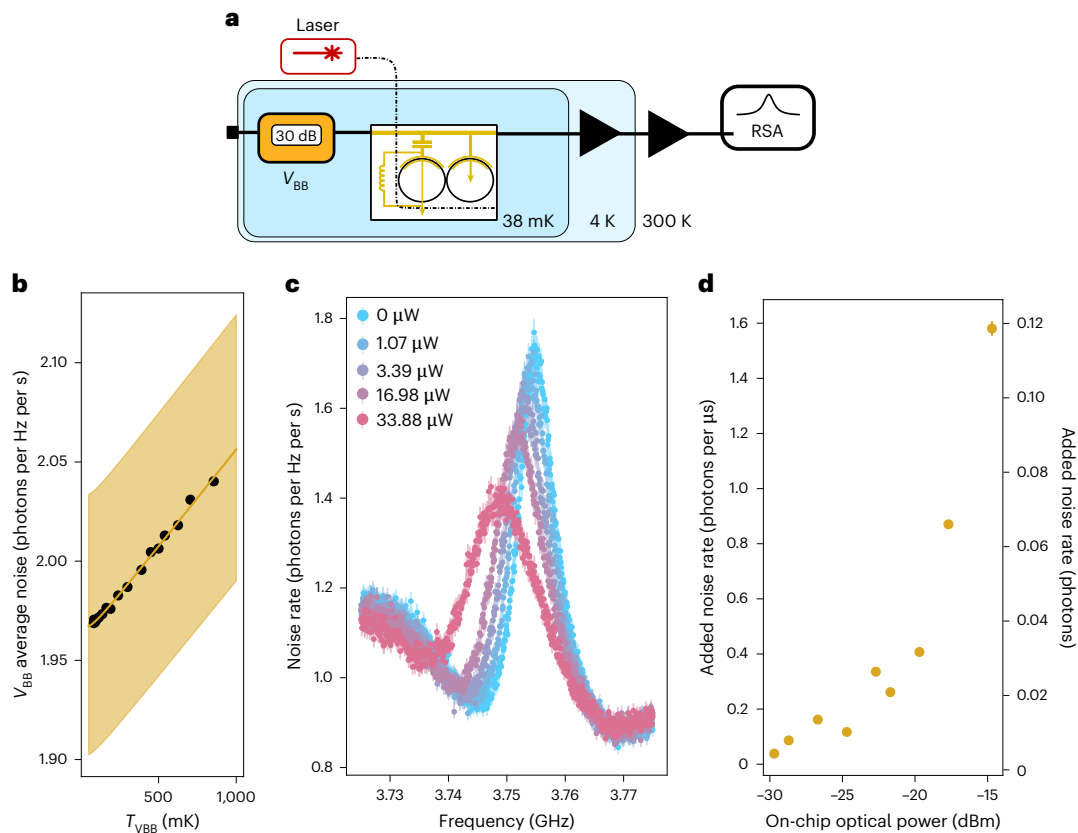
Fig. 4 | Evaluation of optically generated microwave noise in the transducer. **a**, Measurement schematic. We sent a CW optical pump to the transducer and measured the PSD (P_{RSA}) of the microwave signal generated on our superconducting electrodes on an RSA with a 1 kHz resolution bandwidth averaging over 200 measurements. We note that the microwave signal was amplified at the 4 K and 300 K temperature stages. We calibrated the link gain in the system using a variable temperature black-body source (V_{BB}) that was weakly thermalized to the mixing chamber plate[22]. **b**, Calibration curve for the average

output noise photon rate per hertz bandwidth of the V_{BB} (black dots) which allowed us to extract G and N_{sys} according to equation (1). The line of best fit is plotted in gold. The fit uncertainty is shaded. **c**, PSD emitted by the device and converted into noise photon rate. Error bars correspond to calibration uncertainty. The PSD measured with the laser beam blocked is plotted in blue. **d**, Added noise rate per microsecond (left axis) and noise photons emitted by the resonator during the resonator lifetime (right axis) for a given CW pump power. The error bars correspond to the uncertainty due to calibration errors plotted in **b**.

(Fig. 4a). The black-body source was weakly thermalized to the mixing chamber plate, so the bath temperature remained less than 10% of the temperature of the black-body source. From equation (1), we extracted $G = 88.45 \pm 0.07$ dB and $N_{sys} = 112 \pm 1.89$ photons for a noise bandwidth BW = 30 MHz, selected to account for broadband added noise contributions. We attribute the high added system noise photon number to the high temperature of our black-body source, added noise of amplifiers at 4 K and 300 K, and reflections from our amplifier at 4 K due to the lack of isolation before the device.

After calibration, we characterized the transducer-added noise (n_{add}) under CW optical excitation by measuring the device output PSD (Fig. 4c). After each RSA measurement, we measured the transmission of our microwave resonator using a vector network analyser (VNA) before increasing the optical power to extract the microwave resonator lifetime at the measured pump power (Extended Data Fig. 4b). We then extracted the added noise photon generation rate for a given CW optical-pump power by integrating the measured PSD over our measurement bandwidth (30 MHz) and normalizing this to the PSD measured when the laser was shuttered (Fig. 4d, left axis). We also estimated the added noise photons taking into account our microwave resonator bandwidth (Fig. 4d, right axis), and we observed low ($n_{add} < 0.118 \pm 0.002$) transducer-generated noise photons for up to 33.88 µW CW optical power. In general, we expected the Purcell-limited coherence time of a transmon qubit to be proportional to the fractional added noise. Thus, we expected the fractional noise photons

generated by the transducer to result in a corresponding penalty to the Purcell-limited coherence time of a qubit.

Transducer–qubit interconnect

We used the transducer to control a SC qubit using microwave signals generated by the transducer from optical inputs. Here, we drove an aluminium split-transmon qubit through the readout resonator. We operated the transducer in a classical red-pumping regime to coherently convert an optical tone (idler) into a microwave tone in an interaction mediated by a strong optical pump using the pulse sequence depicted in Fig. 5a. Here, an arbitrary-waveform generator triggered by the qubit control board (radio frequency system on a chip (RFSoC)) was used to gate the optical pulses used to generate the microwave drive signal. The RFSoC then sent a readout pulse to the qubit's readout resonator to measure the qubit state after excitation.

We applied square optical pulses of length (τ_p) that were much longer than the optical resonator linewidth ($1/\kappa_{\pm} \approx 15$ ns, $\tau_p > 70$ ns), which approximates an asymmetric Gaussian output microwave pulse (Supplementary Section 3). For each measurement, we used a 100 µs repetition time between events to be consistent with baseline traditional radio frequency (RF) qubit measurements (Extended Data Fig. 5) while maintaining a low bath temperature ($T \approx 14$ mK).

We performed qubit spectroscopy and Rabi oscillation measurements. We first performed CW qubit spectroscopy using a CW microwave tone generated by the transducer ($\omega_{MW}/2\pi = 3.703$ GHz) to excite
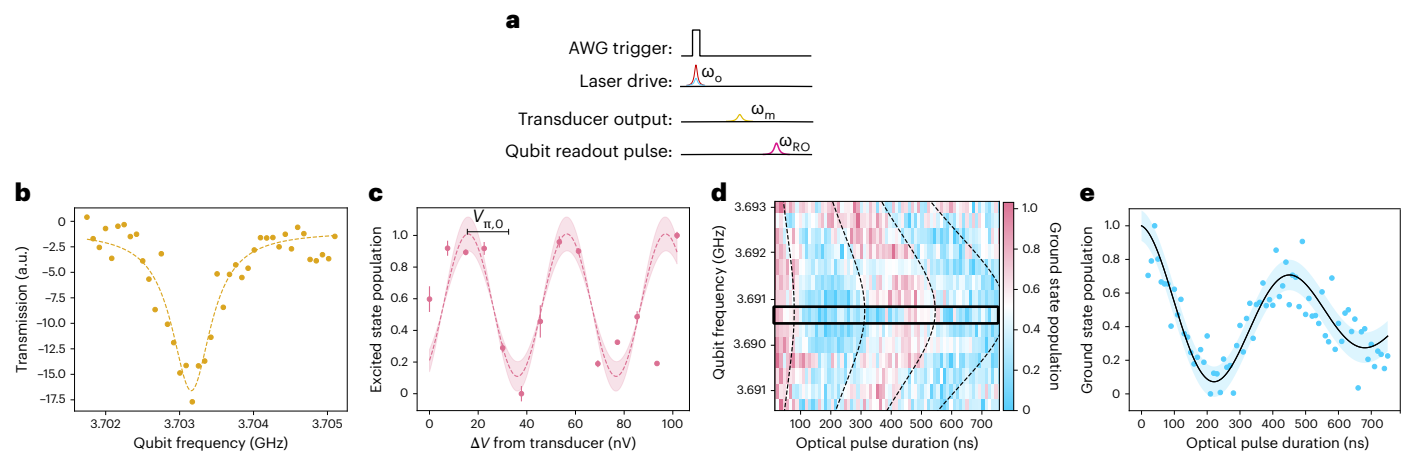
Fig. 5 | Optical control of superconducting qubits. a, Pulse sequence for pulsed transducer-driven qubit measurements. A trigger was sent from the room-temperature qubit control electronics to the arbitrary waveform generator used to generate the optical pulses. Optical pulses at the transducer generated a microwave pulse of approximately equal pulse width. The pulse was sent to the qubit, after which a readout pulse was generated at room temperature, transmitted through the qubit readout resonator and measured to extract the qubit state. See Supplementary Section 4 for full details. **b**, CW qubit spectroscopy using ~328 nV microwave signal generated by the transducer. Flux biasing of the qubit was used to sweep the qubit frequency into resonance with the transducer signal. The population was read out by means of the dispersively coupled readout resonator. **c**, Optically driven qubit power-Rabi oscillations using the pulse sequence described in **a** with 100 ns pulses. The optical on-chip pump power was kept constant at $P_{pk} = 7 \pm 0.5\,\mu W$. The optical power of the idler was swept from 400 to 500 nW, which corresponded to qubit drive voltages from

856 to 958 nV. Error bars on the population correspond to uncertainties when projecting data onto a phase-quadrature axis. From our measurements, we fit the Rabi oscillation and evaluated a Rabi π-pulse amplitude $V_\pi \propto 20.28 \pm 0.035$ nV satisfied for integer multiples of $V_{\pi,n}$. The fitting error is shaded in pink. **d–e**, Optically driven qubit time-Rabi oscillations. We fixed the power in the optical pump and idler and swept the width of the optical pulses to measure the corresponding change in qubit population. We flux biased the qubit to sweep the detuning of the qubit from the optically generated microwave tone in a characteristic chevron profile (**d**). Dotted lines are the theoretical prediction of Rabi frequency as a function of detuning following $\Omega'_R = \sqrt{\Omega_R^2 + \delta^2}$, where Ω'_R is the Rabi frequency at detuning δ given resonant Rabi frequency Ω_R. The population for different pulse widths near the optimal bias is shown in **e**, for which we measured a Rabi frequency of 2.27 MHz by fitting a Rabi oscillation with a time decay. Error bars on the population correspond to uncertainties when projecting data onto a phase-quadrature axis. The fitting error is shaded in blue.

the qubit population (Fig. 5b) and verify excitation transfer between the transducer and the qubit and determine the transducer output power needed to excite the qubit.

Next, we performed Rabi oscillation measurements in the power (Fig. 5c) and time (Fig. 5d–e) domains and extracted parameters needed to impart a π pulse to the qubit. For optically driven qubit power-Rabi measurements, we kept an optical pulse width of 100 ns ($\omega_{MW}/2\pi = 3.71$ GHz) and uniform pump power ($P_{\omega_-} = 7 \pm 5\,\mu W$) while linearly increasing the optical power in the blue sideband (P_{ω_+}) arriving at the transducer to linearly increase the microwave power arriving at the qubit (Fig. 5c). This resulted in a π-pulse voltage amplitude $V_\pi = 20.28$ nV, extracted by fitting the Rabi oscillations and assuming a 50 Ω load at the qubit. Some output power instability (>3 dB measured before and after some successive measurements) due to power-dependent drifts in our system motivated further measurements in the time-Rabi domain to maintain more uniform power at our single-sideband modulator and device.

For optically driven time-Rabi measurements (Fig. 5d,e), we maintained uniform pump and idler power ($P_{pump} \approx 7 \pm 0.5\,\mu W$, $P_{idler} \approx 700 \pm 150$ nW) and swept the optical pulse width to change the width of the microwave pulse ($\omega_{MW}/2\pi = 3.6909$ GHz) arriving at the qubits. We attributed the lower operating frequency used here, as compared with the frequency reported previously, to thermal effects in our system or the operation of the transducer away from the triple-resonance condition.

The flux bias was swept to bias the qubit to different frequencies to measure the qubit excitation relative to the transducer frequency in a chevron-type measurement, where the Rabi frequency (Ω'_R) changed as a function of detuning δ by $\Omega'_R = \sqrt{\Omega_r^2 + \delta^2}$ (dotted lines in Fig. 5d). We fit the Rabi oscillations according to $P_{Rabi} = Ae^{-t/\tau}\sin(2\pi t/(2T_\pi)) + P_b$ to extract a π shift to the qubit state for pulse width T_π, characteristic decay τ and offset P_b, and measured $T_\pi \propto 220$ ns with

$\Omega_R/2\pi = 2.27$ MHz at the transducer frequency. Because the Rabi frequency was proportional to the incident microwave pump power, we could compare the measured Rabi frequency with the estimated transducer microwave output power (Methods) to estimate 46% signal loss between the transducer and qubit. We attributed this high loss to microwave losses in the cables, circulators, filters and the directional coupler between the transducer and the qubit due to a bandwidth mismatch between our operating frequency and cryogenic electronics. Measured system losses are summarized in Methods.

We measured a Rabi decay constant of $\tau = 600 \pm 200$ ns. From transducer-generated added noise reported in Fig. 4d, we estimated that the transducer operating at 7 μW peak optical power resulted in $n_{add} < 0.02$ added noise photons during optically driven qubit measurements, resulting in a 2% transducer-noise penalty on the Purcell-limited qubit coherence time ($T_{MOQT} = \frac{1}{\gamma(n_{add}+1)}$). We used RF measurements conducted with the RFSoC to estimate the qubit decay constant $\gamma = 1.936$ kHz (Methods). This allowed us to estimate a transducer-limited coherence time of 82 μs. This value is an underestimate, because the thermalized components in the interconnect will decrease the amount of thermal noise that reaches the qubits. The transducer-limited coherence time is much greater than our measured $\tau_{Rabi} = 600 \pm 200$ ns and $T_2^* = 710 \pm 5$ ns measured during baseline coherence measurements; therefore, we conclude that our qubit coherence times are likely to be limited by other environmental noise sources.

Discussions and outlook

We demonstrate a CEO-MOQT with high per-microwatt conversion efficiency in the linear regime of our SC resonator ($\%\eta/\mu W = 0.05$), driven with up to 44 μW for a peak efficiency $\eta = 1.18\%$, cooperativity $C = 1.16\%$ and microwave–optical single-photon coupling rate $g_{eo}/2\pi = 945$ Hz, used for coherent optical driving of a SC qubit. Furthermore, we report low added microwave noise from operating the

device, with $\bar{n}_{add} < 0.12$ photons for up to 33 μW on-chip optical power. More than an order of magnitude improvement in device performance could be made by reducing microwave losses, using a single-ended microwave resonator fabricated directly on the Si handle wafer (instead of on SiO_2) and by reducing the optical coupling losses to minimize scattering and to leverage the full incident pump power on-chip. Improvements to the microwave extraction efficiency and total link loss between the transducer and qubits will be essential to realize high-fidelity quantum information transfer in the future.

The increased optical bandwidth compared with the microwave domain can be leveraged with a flux tunable microwave cavity[19]. Measurement improvements, such as a phase lock loop between the qubit readout electronics (or future transducers at the readout frequency) and the pump driving tone can enable phase control of the qubits and more intricate gate operations between qubit nodes. By engineering the temporal profile of optical-pump fields, we can generate shaped, symmetric single-microwave photons to achieve high-efficiency photon transfer between the transducer and a qubit device (Supplementary Section 3). Finally, the low microwave noise generation when continuously pumping the device indicates that stronger optical-pump fields can be used for conversion without affecting qubit performance within the errors of baseline measurements (Extended Data Fig. 7). Characterizing the link between the transducer and qubits with higher coherence time devices will allow us to better quantify the effect of the CEO-MOQT on SC qubit performance.

Although the CEO-MOQT discussed in this article operates in the low cooperativity regime with modest conversion efficiency, the device performance shows potential for networking SC qubits using heralded remote-entanglement protocols when operating in the spontaneous parametric down-conversion regime[5,38]. This can enable the scaling of processors across multiple cryostats, eliminating volumetric constraints that currently exist in these systems. Combining this with the work presented here, as well as with recent demonstrations of optical readout of SC qubits[29,30], provides a path towards forming all-optical interfaces with SC qubits to facilitate the extension of SC quantum systems to enable large scale quantum processors[39,40].

Online content

Any methods, additional references, Nature Portfolio reporting summaries, source data, extended data, supplementary information, acknowledgements, peer review information; details of author contributions and competing interests; and statements of data and code availability are available at https://doi.org/10.1038/s41567-025-02812-0.

References

1.   Arute, F. et al. Quantum supremacy using a programmable superconducting processor. *Nature* **574**, 505–510 (2019).
2.   Kim, Y. et al. Evidence for the utility of quantum computing before fault tolerance. *Nature* **618**, 500–505 (2023).
3.   Gambetta, J. M., Chow, J. M. & Steffen, M. Building logical qubits in a superconducting quantum computing system. *npj Quantum Inf.* **3**, 1–7 (2017).
4.   Krinner, S. et al. Engineering cryogenic setups for 100-qubit scale superconducting circuit systems. *EPJ Quantum Technol.* **6**, 1–29 (2019).
5.   Krastanov, S. et al. Optically heralded entanglement of superconducting systems in quantum networks. *Phys. Rev. Lett.* **127**, 040503 (2021).
6.   Zhong, C., Han, X. & Jiang, L. Microwave and optical entanglement for quantum transduction with electro-optomechanics. *Phys. Rev. Appl.* **18**, 054061 (2022).
7.   Storz, S. et al. Loophole-free Bell inequality violation with superconducting circuits. *Nature* **617**, 265–270 (2023).
8.   Lecocq, F. et al. Control and readout of a superconducting qubit using a photonic link. *Nature* **591**, 575–579 (2021).
9.   Bersin, E. et al. Development of a Boston-area 50-km fiber quantum network testbed. *Phys. Rev. Appl.* **21**, 014024 (2024).
10. Reiserer, A., Kalb, N., Rempe, G. & Ritter, S. A quantum gate between a flying optical photon and a single trapped atom. *Nature* **508**, 237–240 (2014).
11. Lauk, N. et al. Perspectives on quantum transduction. *Quantum Sci. Technol.* **5**, 020501 (2020).
12. Clerk, A. A., Lehnert, K. W., Bertet, P., Petta, J. R. & Nakamura, Y. Hybrid quantum systems with circuit quantum electrodynamics. *Nat. Phys.* **16**, 257–267 (2020).
13. Han, X., Fu, W., Zou, C.-L., Jiang, L. & Tang, H. X. Microwave-optical quantum frequency conversion. *Optica* **8**, 1050 (2021).
14. Jiang, W. et al. Efficient bidirectional piezo-optomechanical transduction between microwave and optical frequency. *Nat. Commun.* **11**, 1166 (2020).
15. Weaver, M. J. et al. An integrated microwave-to-optics interface for scalable quantum computing. *Nat. Nanotechnol.* **19**, 166–172 (2024).
16. Mirhosseini, M., Sipahigil, A., Kalaee, M. & Painter, O. Superconducting qubit to optical photon transduction. *Nature* **588**, 599–603 (2020).
17. Brubaker, B. et al. Optomechanical ground-state cooling in a continuous and efficient electro-optic transducer. *Phys. Rev. X* **12**, 021062 (2022).
18. Sahu, R. et al. Entangling microwaves with light. *Science* **380**, 718–721 (2023).
19. Xu, M., Han, X., Fu, W., Zou, C.-L. & Tang, H. X. Frequency-tunable high-Q superconducting resonators via wireless control of nonlinear kinetic inductance. *Appl. Phys. Lett.* **114**, 192601 (2019).
20. Holzgrafe, J. et al. Cavity electro-optics in thin-film lithium niobate for efficient microwave-to-optical transduction. *Optica* **7**, 1714–1720 (2020).
21. McKenna, T. P. et al. Cryogenic microwave-to-optical conversion using a triply resonant lithium-niobate-on-sapphire transducer. *Optica* **7**, 1737–1745 (2020).
22. Hease, W. et al. Bidirectional electro-optic wavelength conversion in the quantum ground state. *PRX Quantum* **1**, 020315 (2020).
23. Xu, Y. et al. Bidirectional interconversion of microwave and light with thin-film lithium niobate. *Nat. Commun.* **12**, 4453 (2021).
24. Meesala, S. et al. Non-classical microwave-optical photon pair generation with a chip-scale transducer. *Nat. Phys.* **20**, 871–877 (2024).
25. Jiang, W. et al. Optically heralded microwave photon addition. *Nat. Phys.* **19**, 1423–1428 (2023).
26. Fan, L. et al. Superconducting cavity electro-optics: a platform for coherent photon conversion between superconducting and photonic circuits. *Sci. Adv.* **4**, eaar4994 (2018).
27. Andrews, R. W. et al. Bidirectional and efficient conversion between microwave and optical light. *Nat. Phys.* **10**, 321–326 (2014).
28. Delaney, R. D. et al. Superconducting-qubit readout via low-backaction electro-optic transduction. *Nature* **606**, 489–493 (2022).
29. van Thiel, T.C. et al. Optical readout of a superconducting qubit using a piezo-optomechanical transducer. *Nat. Phys.* **21**, 401–405 (2025).
30. Arnold, G. et al. All-optical superconducting qubit readout. *Nat. Phys.* **21**, 393–400 (2025).
31. Zhang, M., Wang, C., Cheng, R., Shams-Ansari, A. & Lončar, M. Monolithic ultra-high-Q lithium niobate microring resonator. *Optica* **4**, 1536–1537 (2017).
32. Shams-Ansari, A. et al. Reduced material loss in thin-film lithium niobate waveguides. *APL Photonics* **7**, 081301 (2022).
33. Luke, K. et al. Wafer-scale low-loss lithium niobate photonic integrated circuits. *Opt. Express* **28**, 24452–24458 (2020).

34. Soltani, M. et al. Efficient quantum microwave-to-optical conversion using electro-optic nanophotonic coupled resonators. *Phys. Rev. A* **96**, 043808 (2017).

35. Zhang, M. et al. Electronically programmable photonic molecule. *Nat. Photon.* **13**, 36–40 (2019).

36. Krantz, P. et al. A quantum engineer's guide to superconducting qubits. *Appl. Phys. Rev.* **6**, 021318 (2019).

37. Holzgrafe, J. et al. Relaxation of the electro-optic response in thin-film lithium niobate modulators. *Opt. Express* **32**, 3619–3631 (2024).

38. Duan, L.-M., Lukin, M. D., Cirac, J. I. & Zoller, P. Long-distance quantum communication with atomic ensembles and linear optics. *Nature* **414**, 413–418 (2001).

39. Lago-Rivera, D., Grandi, S., Rakonjac, J. V., Seri, A. & de Riedmatten, H. Telecom-heralded entanglement between multimode solid-state quantum memories. *Nature* **594**, 37–40 (2021).

40. Bhaskar, M. K. et al. Experimental demonstration of memory-enhanced quantum communication. *Nature* **580**, 60–64 (2020).

Methods

Fabrication

Devices were fabricated on 600-nm x-cut TFLN bonded on 4,700 nm of thermally grown oxide on a silicon carrier (NanoLN). The waveguides were defined using negative-tone hydrogen silsesquioxane (HSQ) (FOx-16) by means of electron-beam lithography under 4× multipass exposure (Elionix F-125). The pattern was then transferred to LN through a physical etching process using Ar$^+$ ions to form a 325-nm ridge waveguide. We further confirmed the thickness of the remaining film using an optical profiler (Filmetrics). We used a wet chemical process to clean the resist and redeposited material after the physical etching. The chip was then cladded with 1.4 μm of inductively coupled plasma-enhanced chemical vapour deposition (IC-PECVD) SiO$_2$. Windows were etched into the cladding oxide and waveguide slab before 40 nm of Nb was sputtered onto the chip. The microwave layer was then defined with positive tone propyleneglycol monomethyl etheracetate photoresist (SPR 700-1.0) by means of optical lithography (Heidelberg 150) and transferred to the Nb film using a CF$_4$ physical etch. The etch depth was targeted to be 100 nm to ensure that the microwave resonator was fully defined.

Transduction efficiency

We characterized the on-chip conversion efficiency by comparing the output signal flux with the input idler flux. In the following section, we describe measurement in the optical-to-microwave conversion regime: an equivalent process was used to characterize microwave-to-optical conversion, with MW (ω_m) → optical (ω_+).

For optical-to-microwave transduction experiments, we characterized the on-chip transduction efficiency by measuring the microwave signal power converted from our optical idler through the qubit transmission line. During these experiments, the qubits were detuned from the transducer frequency by >500 MHz. We pumped the device with a laser (P_{pump}) resonant with our red optical sideband (ω_-) and optical idler at ω_+, generated at room temperature ($P_{in,opt}$). After the device, we measured the microwave power generated at ω_{MW} at room temperature ($P_{out,MW}$). From this, we found the input flux of the signal $\Phi_{MW,opt} = \frac{P}{\hbar\omega_{MW,opt}}$. We measured optical losses at room temperature with a powermeter (Thorlabs PM100D) calibrated against an integrating sphere (Thorlabs S140C). It was assumed that optical losses in our measurement network remained nominally constant throughout the experiment. We calibrated our microwave losses as described in Methods to determine our input optical loss $\eta_{in,opt}$ and output optical loss $\eta_{out,opt}$. Finally, we calculated our on-chip conversion efficiency (η_{MOQT}) by normalizing the idler and signal losses at room temperature to our input and output losses according to

$$\eta_{MOQT} = \eta_{MW \to optical} = \eta_{optical \to MW} \tag{2}$$

$$\eta_{MW \to optical} = \frac{1}{\eta_{in,MW}\eta_{out,optical}} \frac{\Phi_{optical}}{\Phi_{MW}} \tag{3}$$

$$\eta_{optical \to MW} = \frac{1}{\eta_{in,optical}\eta_{out,MW}} \frac{\Phi_{MW}}{\Phi_{optical}} \tag{4}$$

The system losses were converted to decibel units (dB) and reported in Table 1. The microwave input and output loss calibration, as well as the transducer–qubit link loss ($\eta_{MOQT\text{-}qubit}$) and estimated qubit RF control input loss ($\eta_{qubit\text{-}in}$).

Microwave loss calibration

The input and output optical losses ($\eta_{in,optical}, \eta_{out,optical}$) were measured at room temperature with fibre transmission measurements as described in the previous section. We could not characterize our microwave losses with room-temperature transmission measurements because the

Table 1 | Link input and output microwave and optical losses measured in our system.

Loss parameter	Link loss (dB)
$\eta_{in,MW}$	−75.49
$\eta_{out,MW}$	+48.99
$\eta_{in,opt.}$	−14.69
$\eta_{out,opt}$	+5.51
$\eta_{sys,MW}$	−26.5
$\eta_{MOQT\text{-}qubit}$	−2.67
$\eta_{qubit\text{-}in}$	−10

We had amplifiers on the microwave and optical outputs, resulting in gain on the system outputs.

system was under vacuum and was sensitive to thermal fluctuations. However, we could calibrate our microwave losses using low-power bidirectional transduction measurements to determine the true on-chip conversion efficiency and our input and output microwave losses.

In addition, we measured the total microwave link loss ($\eta_{sys,MW}$) using microwave transmission measurements. This allowed us to characterize our microwave input and output losses as $\eta_{sys,MW}(dB) = \eta_{in,MW}(dB) + \eta_{out,MW}(dB)$ and extract our link loss when we solve this with equations (2)–(4) given that we only probe $\eta_{in,MW}$ during MW → optical conversion and $\eta_{out,MW}$ for optical → MW conversion.

Transducer–qubit link loss. The calibration described above allowed us to extract the microwave losses before and after the transducer. It did not provide any information regarding the link loss between the transducer and qubit ($\eta_{MOQT\text{-}qubit}$).

However, the transducer output microwave loss included the loss through the qubit transmission line. Because the Rabi frequency (Ω_R) was proportional to the total power ($P = \int P_{pk}\,dt$ for a peak power P_{pk}), we could use Rabi measurements to extract the link loss between the transducer and qubits. For a qubit with decay constant γ at frequency ω_q, the Rabi frequency is given by

$$\Omega_R = 2\sqrt{\frac{\gamma P}{\hbar\omega_q}} \tag{.5}$$

First, we needed to extract the qubit decay constant γ using the RF calibration from the RFSoC. Here, Gaussian pulses were generated (that is, $P = \int P_{pk}\,dt \to \sqrt{2\pi\sigma^2}P_{pk}$) for pulse width σ at room temperature before being sent to the fridge. For RFSoC time-Rabi measurements, we measured a room-temperature pulse amplitude of 179.69 μV and estimated overall a −10 dB link loss between the RFSoC and qubits (including 3 dB propagation losses, 58 dB amplification and 66 dB attenuation). This allowed us to extract a qubit decay constant of $\gamma/2\pi = 1.936$ kHz.

We used the extracted decay constant to estimate the transducer–qubit link loss ($\eta_{MOQT\text{-}qubit}$) by comparing the measured Rabi frequency ($\Omega_{R,measured}$) with the expected Rabi frequency ($\Omega_{R,expected}$) for the normalized power we measured being emitted at the transducer ($P_{MOQT,MW}$), as

$$\frac{\Omega_{R,measured}}{\Omega_{R,expected}} = \sqrt{\frac{P_{qubit}}{P_{on\text{-}chip,MW}}} \tag{6}$$

for microwave power at the qubit P_{qubit}, where $P_{qubit} = \eta_{MOQT\text{-}qubit}P_{on\text{-}chip,MW}$ or

$$\eta_{MOQT\text{-}qubit} = \left(\frac{\Omega_{R,measured}}{\Omega_{R,expected}}\right)^2 \tag{7}$$

From our microwave loss calibration, we expected −114.5 dBm to be emitted by the transducer in an asymmetric Gaussian of width

$1/\tau$ for square optical pulses of length τ and a tail determined by the microwave decay κ_{MW}. Here, we approximated the total power $\Sigma P = \int P \mathrm{d}t = P(\sqrt{\pi}\tau + (1 - 1/\kappa_{MW}))$. This resulted in an expected Rabi frequency of $\Omega_{R,measured}/2\pi = 4.20$ MHz, which we compared with our measured Rabi frequency $\Omega_{R,measured}/2\pi = 2.27$ MHz. We estimated 2.67 dB (46%) loss between the transducer and qubits. We attributed this largely to propagation losses through system components (coaxial cable, filters, circulators and directional coupler) between the transducer and qubits. For off-resonant drive, such as the chevron measurement in Fig. 5d, we expected to measure a roll-off in Rabi frequency

$$\Omega'_R = \sqrt{\Omega_R^2 + \delta^2} \tag{8}$$

where δ is the detuning between the qubit frequency and the driving tone.

Transducer measurement

For independent transducer measurements, a Santec TSL-550 CL band laser operated around 1,530 nm was sent to a single-sideband EO modulator. For optical-to-microwave conversion experiments, the modulator was weakly driven by a vector network analyser (VNA) at the transducer microwave resonator frequency to generate an optical sideband. For microwave–optical conversion experiments, the VNA output was switched to the dilution refrigerator input and used to apply a weak microwave idler to the transducer. The optical pump(s) could be switched to an acousto-optic modulator and electro-optic modulator for phase locking the optical pump laser to the optical resonator using the Pound–Drever–Hall technique. A d.c. bias was applied to the transducer bias capacitor by applying a d.c. voltage to a cryogenic bias-tee (QMC-CRYOTEE-0.218SMA) using a Keithly 2400 power supply.

Noise measurement

The noise measurement was performed after the qubits were removed from the set-up and bypassed cryogenic circulators, amplifiers and filters below 4 K, with amplification stages at 4 K and room temperature. The variable black-body source (V_{BB}) was constructed from a 30-dB attenuator thermalized to a copper block. The copper block housed a cartridge heater (Lakeshore HTR-50) and temperature sensor (Lakeshore RX-102B-RS) that allowed us to apply voltage-dependent temperature changes to our microwave input line. The V_{BB} was weakly thermalized to the mixing chamber plate using a polymer spacer, which allowed us to heat the waveguide to ~1 K while maintaining a mixing-plate temperature <100 mK. The high added base temperature resulted in a large added noise photon number. The heater was terminated for optically pumped noise measurements. Off-resonant laser power was sent through the device by means of a fibre array coupled to on-chip grating couplers.

Qubit control

Qubit control was implemented using the Xilinx ZCU111+ RFSoC with control built using the open-source Quantum Instrument Control Kit (QICK). Qubits could be characterized independently from the transducer by sending in control pulses on a directional coupler after the transducer chip to give a baseline for qubit measurements using 50 ns pulses with 100 µs repetition rate averaged over 1,000 experimental shots. This allowed us to establish a baseline for qubit lifetimes (T_1), coherence times (T_2^*) and RF readout fidelities.

Optically driven qubit measurements

In transducer-driven power-Rabi measurements, output power was swept from −108.33 to −107.36 dBm for 100 ns pulse-width measurements and converted to voltage units assuming a 50 Ω load. Here, measurements were averaged over 1,000 experimental shots.

For transducer-driven time-Rabi measurements, output power was held fixed at −115.8 ± 0.4 dBm. Power was regularly checked on a VNA between each frequency flux bias to verify that the transducer bias had not drifted. Here, measurements were averaged over 5,000 experimental shots.

Data availability

Data shown in the main text (Figs. 2–5) and Extended Data Figs. 1–7 are available via Zenodo at https://doi.org/10.5281/zenodo.14628434 (ref. 41).

References

41. Warner, H. et al. Data for 'coherent control of a superconducting qubit using light'. *Zenodo* https://doi.org/10.5281/zenodo.14628434 (2025).

Author contributions

J.H. and H.K.W. designed the transducer. D.B., H.K.W., J.H. and C.J.X. fabricated the transducer with help from E.B. and M.C. for the Nb superconductor growth and A.S.-A. for fabrication development. Superconducting qubits were designed and fabricated by Rigetti Computing. H.K.W. built the experimental set-up with help from J.H. and B.Y. Measurements were designed by H.K.W., B.Y. and J.H. with help from S.P., N.S., D.Z., E.S., B.L., L.J., M.J.R. and M.L. The cryogenic measurement system was built and maintained by H.K.W., J.H., N.S., D.Z. and G.J. Measurements and data analysis were completed by H.K.W. H.K.W. wrote the manuscript with contributions from all authors.

Competing interests

J.H. and M.L. are currently involved in developing lithium niobate technologies at HyperLight Corporation. B.Y., S.P., E.S., B.L. and M.J.R. are or have been involved in developing quantum computing technology at Rigetti Computing. The remaining authors declare no competing interests.
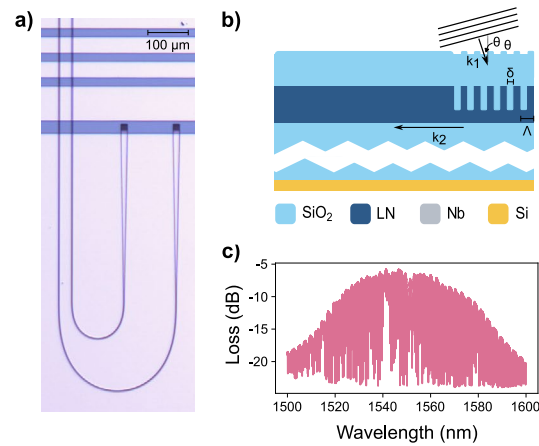
Additional information

Extended data is available for this paper at https://doi.org/10.1038/s41567-025-02812-0.

Extended Data Fig. 1 | Transducer grating couplers. (**a**) Optical micrograph of grating couplers etched in TFLN cladded with SiO_2. A Nb alignment grating is created around the couplers in order to help with coupling inside of the dilution refrigerator. (**b**) Cross section of grating couplers for transducer material stack. Light is coupled into the waveguide according to the phase matching condition $k_2 = k_1 \sin\theta + 2\pi n_{eff}/\Lambda$ where $k = 2\pi/\Lambda$ is the wave-vector in the material propagating at angle θ and gratings are described by pitch Λ and separation δ. (**c**) Loss per grating measured through our device.
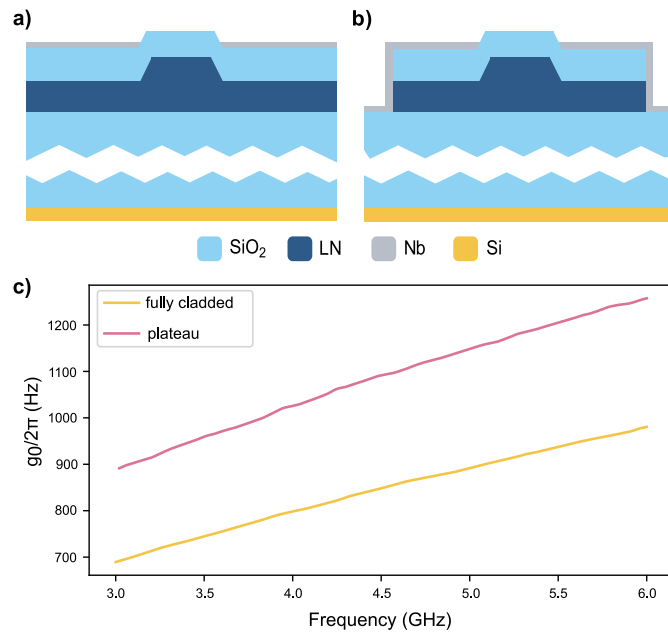
Extended Data Fig. 2 | Electro-optic coupling rate. We simulate the microwave-optical single photon coupling rate, g_0, for (**a**) fully cladded and (**b**) plateau etch electrode geometries. (**c**) We see a 1.4× improvement in single photon coupling rate when comparing the plateau etch to a fully cladded device.
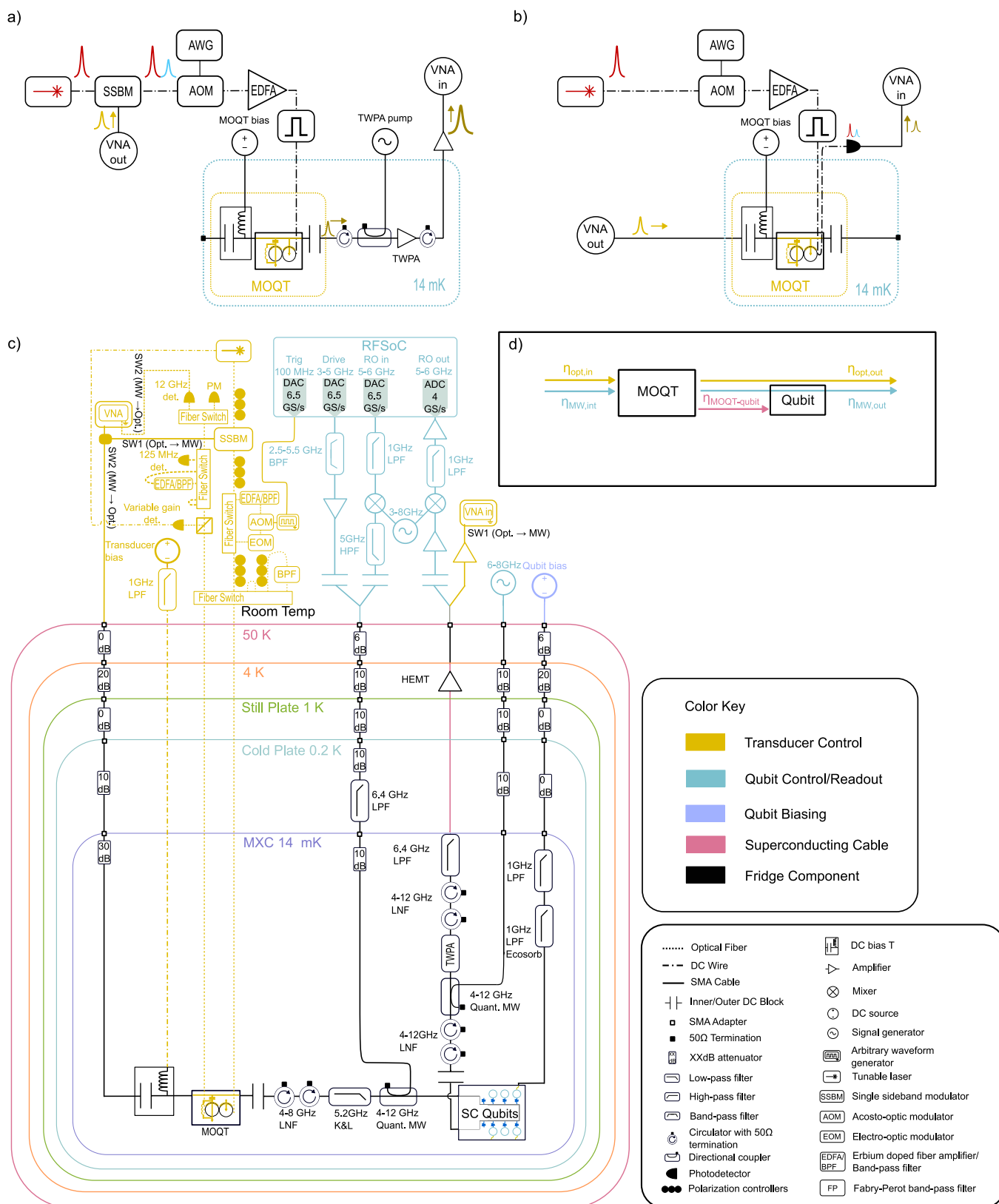
**Extended Data Fig. 3 | Schematic for CEO-MOQT and SC qubit measurements.** (**a**) Simplified schematic for microwave → optical conversion and (**b**) optical → microwave conversion. Here, solid lines correspond to electrical cabling and dotted lines correspond to optical fiber. (**c**) detailed schematic for the whole measurement system. Transducer components are highlighted in gold. Qubit components are highlighted in pink. (**d**) Definition of link losses (η) in the system.
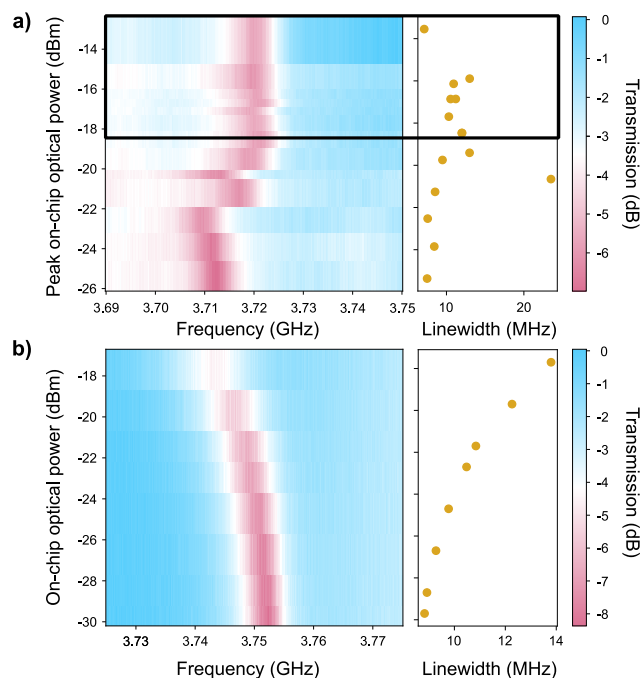
Extended Data Fig. 4 | Microwave resonator spectra and linewidths (plotted in gold) for measured on-chip optical pump powers. (**a**) Microwave characterization during transduction efficiency measurements. Powers measured with pulsed optical pumps are enclosed in a black box. We selected our duty cycle for each pulsed pump power to maintain low thermal bath temperature, which allowed us to maintain a microwave linewidth ~ 10 MHz for our pulsed transduction efficiency measurements. (**b**) Microwave transmission during noise measurements.
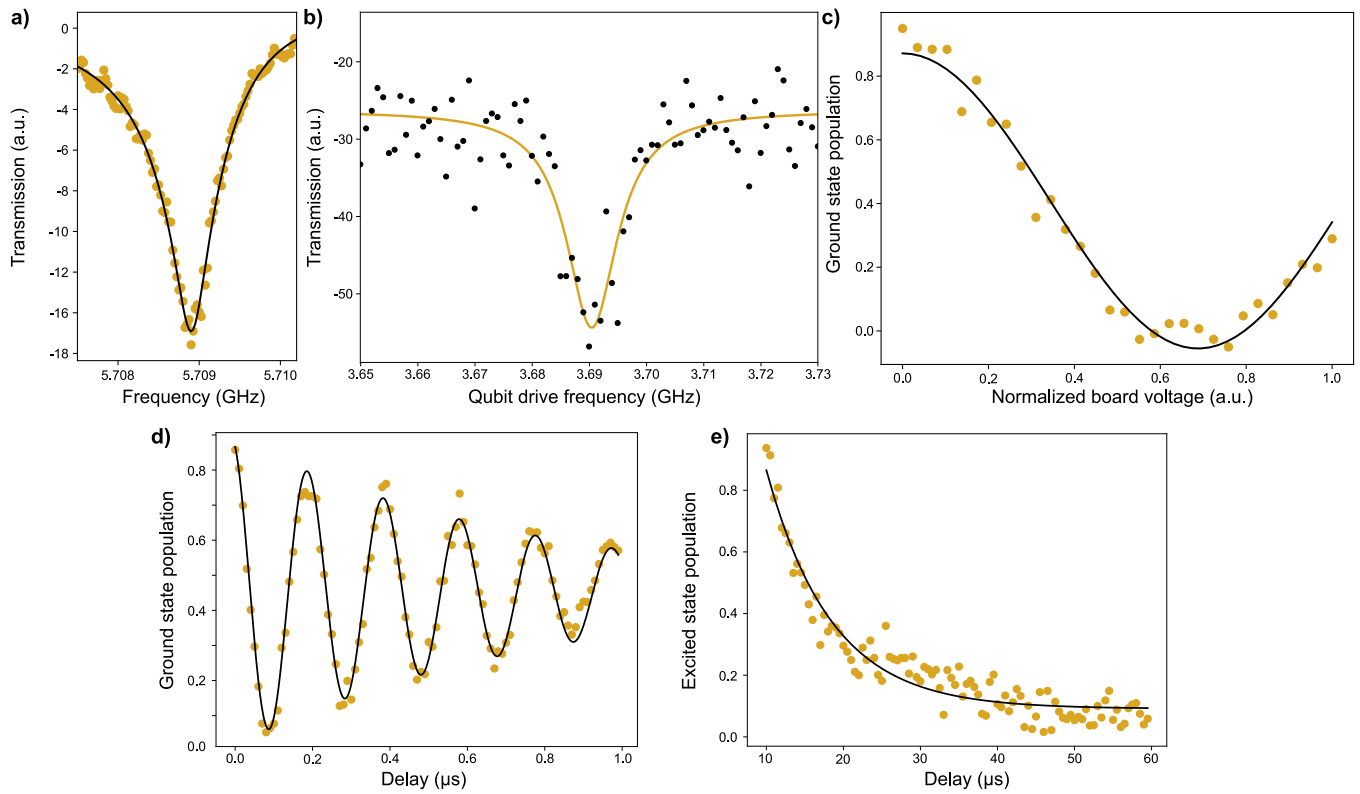
Extended Data Fig. 5 | Summary of all-RF qubit bring-up using power domain π-pulses. We present (**a**) readout resonator transmission at 5.709 GHz, (**b**) qubit spectroscopy when the qubit is flux-biased to 3.690 GHz, (**c**) power Rabi oscillations reported in arbitrary voltage units, (**d**) Ramsey measurements, from which we extract a coherence time $T_2^* = 778$ ns, and (**e**) a lifetime measurement, from which we extract a lifetime of $T_1 = 8.42\,\mu$s.
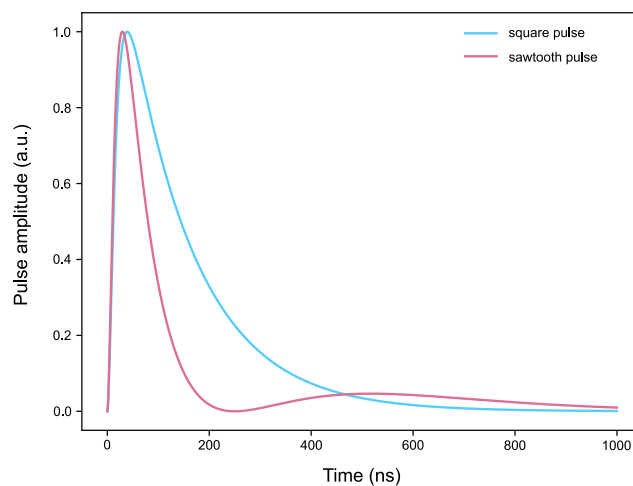
Extended Data Fig. 6 | Simulated microwave emission profiles for 100 ns pulses. Pulse profiles are for square-wave input optical fields (blue) and sawtooth-wave input optical fields (pink).
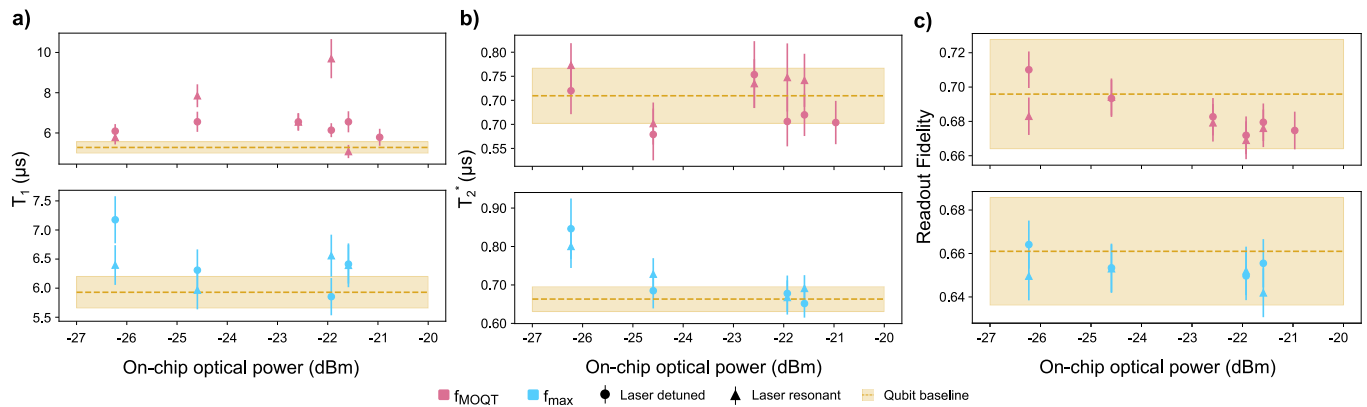
Extended Data Fig. 7 | Qubit performance while transducer is optically pumped. We characterize (**a**) Qubit lifetime (T_1), (**b**) coherence time (T_2^*), and (**c**) readout fidelity as a function of on-chip optical power with a single strong pump field (no optical idler) averaged over 5000 measurements. Errorbars correspond to the standard error over all repetitions. The top (pink) is measured with the qubit flux-biased to the transducer frequency (f_{MOQT}) while the bottom (blue) is measured with the qubit flux-biased to the qubit maximum frequency (f_{max}). We report the T_1, T_2^*, and readout fidelity of the qubit while the laser is off as a dashed gold line, with the confidence interval shaded in gold. We measure the qubit while the laser is off-resonant with our optical modes (circles) and locked to the red optical resonance (triangles). We see that the qubit lifetimes (**a**), coherence times (**b**), and fidelities (**c**) do not experience degradation within the error of baseline measurements with increased optical power at the transducer flux bias ($f_{CEO-MOQT} = 3.71$ GHz) or the qubit maximum frequency ($f_{max} = 4.571$ GHz).